Quantitative comparison of mitotic spindles by confocal image analysis

Jeffery R. Price
Deniz Aykac
Shaun S. Gleason
Oak Ridge National Laboratory
Image Science and Machine Vision Group
Oak Ridge, Tennessee 37831-6010
E-mail: pricejr@ornl.gov

Karuna Chourey
Yie Liu
Oak Ridge National Laboratory
Mammalian Genetics Group
Oak Ridge, Tennessee 37831-6445

Abstract. The mitotic spindle is a subcellular protein structure that facilitates chromosome segregation and is crucial to cell division. We describe an image processing approach to quantitatively characterize and compare mitotic spindles that have been imaged three dimensionally using confocal microscopy with fixed-cell preparations. The proposed approach is based on a set of features that are computed from each image stack representing a spindle. We compare several spindle datasets of varying biological (genotype) and/or environmental (drug treatment) conditions. The goal of this effort is to aid biologists in detecting differences between spindles that may not be apparent under subjective visual inspection, and furthermore, to eventually automate such analysis in high-throughput scenarios (thousands of images) where manual inspection would be unreasonable. Experimental results on positive- and negative-control data indicate that the proposed approach is indeed effective. Differences are detected when it is known they do exist (positive control) and no differences are detected when there are none (negative control). In two other experimental comparisons, results indicate structural spindle differences that biologists had not observed previously. [DOI: 10.1117/1.1955531]

Keywords: image analysis; subcellular imaging; confocal microscopy; fluorescence microscopy; mitotic spindle; gene knockout.

Paper 04061 received Apr. 15, 2004; revised manuscript received Feb. 3, 2005; accepted for publication Feb. 21, 2005; published online Jul. 15, 2005.

1 Introduction

The current state of the art in imaging is capable of providing biologists with tremendous amounts of data that can easily overwhelm any quantitative analysis capabilities of a human. The research we present begins to address the need for automated, quantitative processing of image data in an area of important and currently evolving functional genomics research. Data related to functional genomics research is often captured in image and/or volumetric form by a variety of instruments and techniques. Some examples include traditional optical microscopy, atomic force microscopy,[1] deconvolution microscopy,[2] and laser-scanning confocal microscopy.[3] Presently, much of the analysis of the acquired image data is performed manually and subjectively—a well-trained scientist examines the image and attempts to make qualitative observations concerning its contents relative to what the scientist has seen before. To conduct statistically meaningful experiments, however, it is necessary that many images be produced and analyzed quantitatively, as has been noted for some time.[4] It can be, of course, prohibitively time consuming for a human to manually analyze a large number (i.e., thousands) of images, and virtually impossible for them to do so quantitatively, especially with 3-D data. Hence there is a need for automated image processing and data analysis in many image-related, functional genomics applications. The work we present begins to address that need as it relates to understanding the mitotic spindle.

The mitotic spindle is a crucial structure involved in cell division (mitosis) in eukaryotes (animals, plants, fungi). The spindle is a tubulin-based protein structure, formed during mitosis, that is critical in chromosome segregation, which is the process of splitting duplicated genetic material between two developing daughter cells. A simple illustration of the spindle is shown in Fig. 1. During cell division, spindle microtubules attach to the centers (centromere) of the chromosomes, which are arranged along the cell's equator or *equatorial plate*. The chromosomes, comprising two sister chromatids, split at this point of attachment and are pulled apart by the spindle. The spindle ends, toward which the split chromosomes are pulled, are referred to as the spindle poles. The spindle poles, which are located at opposite ends of the whole cell, are in fact organelles known as centrioles.

Biologists are particularly interested in the mitotic spindle for several reasons. Abnormal function or disruption of the spindle will lead to cell death, abnormal cell growth, and/or genomic instability because of inaccurate chromosome segregation.[5] Inaccurate chromosome segregation can lead to genomic instability, which is a characteristic common to all cancer cells. Furthermore, many anticancer agents (e.g., Taxol or paclitaxel) are actually tubulin poisons that attack the

Address all correspondence to Dr. Jeffery R. Price, Oak Ridge National Laboratory, Image Science and Machine Vision Group, Oak Ridge, TN 37831-6010. Tel: (865)-574-5743; Fax: (865)576-8380; E-mail: pricejr@ornl.gov

1083-3668/2005/10(4)/044012/12/$22.00 © 2005 SPIE

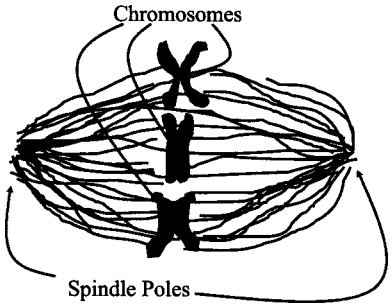

Fig. 1 A simple 2-D illustration of the mitotic spindle. The spindle emanates from the spindle poles and facilitates chromosome segregation. During mitosis (cell division) the separated chromosomes are pulled by the spindle toward the poles into two forming daughter cells. The 3-D shape of the spindle is approximately ellipsoidal.

spindle structure to prevent cell division, which proceeds rampantly in cancer cells.[6] Finally, many proteins interact with the spindle in unknown or poorly understood ways. The principal motivation for the image analysis work we present here is to develop tools that will aid cell biologists in understanding the roles of spindle-associated proteins, and potentially pharmaceutical companies, in searching for novel tubulin poisons or understanding subtle effects of other compounds on the spindle. An improved understanding of protein roles may also help uncover future anticancer drugs and drug targets.

To date, there has been only limited work regarding quantitative 3-D or 4-D (i.e., 3-D plus time-lapse imaging of living cells) imaging of the spindle. Electron tomography[7] has been employed to find the 3-D structure of the early spindle in hopes of uncovering structure-function relationships in mutated yeast. Although this approach provides excellent spatial resolution, the noisy images would be challenging to analyze automatically, and the required manual efforts limit potential high-throughput capabilities. Courtesy of advances in microscopy[8] and imaging techniques,[9] the need for quantitative 3-D (and 4-D) analysis of the spindle has been clearly demonstrated. In fact, 4-D imaging of mitosis has shown that different modes of cell division are linked to 3-D rotations and asymmetric orientation of the spindle body in the fruit fly,[10] the mouse,[11] and in plant cells.[12] 3-D live-cell imaging has also been employed to study the effects of mutations on the mitotic spindle in hopes of uncovering protein interactions.[13] Although some of this previous research has employed quantitative measures,[10,11,14] more extensive and descriptive measures, such as those we present in this work, will significantly improve current methodology. Additional research[12,13] has been primarily qualitative. We note that a succinct version of the research in this work has been previously presented.[15]

The remainder of this work is organized as follows. In Sec. 2, we briefly discuss the cell biology research that motivates our image analysis work. We then turn our attention to the analysis of the images in Sec. 3, where we describe image-based features we have developed to characterize the spindle. Note that the aim here is not one of traditional pattern recognition, where we usually seek to discriminate between different classes. Instead, we seek to define measures or features that can quantify the spindle, and then use those features to compare spindles so that subtle differences might be detected statistically. In other words, the problem at hand is not one of discrimination, but rather quantification and comparison. In Sec. 4, we describe the results of our approach on several datasets of interest, and then we conclude in Sec.5 with a few summary remarks and notes about our future research goals.

2 Biology Background

As noted in Sec. 1, there are many proteins associated with the spindle whose roles are poorly understood or completely unknown. One way that biologists investigate the roles of a protein in cells is to produce and study gene-knockout (KO) organisms, where "knockout" means that a gene is removed from the organism. Since specific proteins are encoded by corresponding genes, the role of a protein can be elucidated by examining the phenotype of the organism deficient in that protein due to gene-KO.

The mouse has been employed as the model organism in this work for several reasons. The mouse is the best-characterized experimental mammal and has the most well-defined genetics of any nonhuman vertebrate. Extensive homologies between mouse and human genomes have been established, thus permitting the mouse to be used as a model system for many human genetic diseases. Finally, both the genome and the embryo of the mouse can be manipulated with relative ease, allowing for an expansion of the genetic resources necessary for functional interpretation of genes and DNA sequences.

The cells used for all imaging studies are known as mouse embryonic fibroblasts, or MEFs. *Primary* and *immortalized* MEFs derived from wild-type (normal) or one of two different knock-out mice are employed. Primary MEFs can only divide in cell culture for a limited period of time. Immortalized cells, on the other hand, have undergone a random mutation (or mutations) and hence gain the capability to continue to divide in culture indefinitely. The two knockout or mutant MEFs employed herein are deficient for either the *p53* gene or the *Vparp* gene. (When italicized, *p53* and *Vparp* refer to genes. When given with capital letters, P53 and VPARP refer to the proteins encoded by those genes.) p53 is a tumor suppressor and its function has been linked to a variety of cellular processes, such as cell cycle control, cell apoptosis (programmed cell death), and transcription activation.[16–18] *p53*-deficient MEFs also exhibit a significantly higher probability of becoming immortalized relative to wild-type MEFs. Vault poly(ADP-ribose) polymerase (VPARP) was originally identified as a minor protein component of the vault ribonucleoprotein (RNP) particle,[19] whose function may be involved in molecular assembly or subcellular transport.[20–22] In addition to its association with cytoplasmic vault particles, subpopulations of VPARP localize to the nucleus and the mitotic spindle, indicating VPARP may have other cellular functions.[19,23] In this study, we are interested to determine if *Vparp* deficiency in mammalian cells can lead to changes in spindle structure.

As a positive control for abnormal spindle characteristics, we treated some immortalized cells (see Sec. 4) with the tubulin poison Taxol (also known as paclitaxel), which is a microtubule depolymerization inhibitor. To function properly, microtubules must be in a dynamic state of polymerization

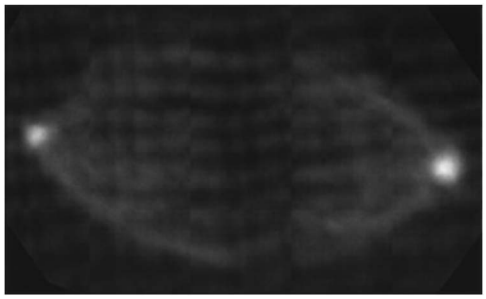

Fig. 2 An example spindle image computed by *z*-sum projection. Note that only the fluorescent-stained tubulin is visible.

and depolymerization.[6] Since the mitotic spindle is composed of microtubules, it is well known that treatment with Taxol will certainly induce structural changes. Taxol is also widely used as an anticancer drug because of its effect on the spindle.

For imaging, fixed-cell (i.e., nonliving) MEFs are employed. These fixed cells were probed with fluorescent, antitubulin antibodies that bind to the tubulin structure of the MEF spindles. The cells were then imaged with a confocal laser scanning microscope to produce 3-D image stacks. An example *z*-sum projection image (i.e., projected to 2-D by summing along the optical axis) is shown in Fig. 2.

3 Image Analysis

In this section, we describe 49 features that are computed for each spindle image stack. These features are intended to compare spindles to one another, as we later describe in Sec. 4, for the purposes of detecting potential differences that are not necessarily apparent to a human observer. The first few features, described in Sec. 3.1, are independent of the spindle shape and are related purely to the distribution of image intensity values in each stack. The remaining features, described in Sec. 3.2, are all related to the spindle morphology.

We note that oftentimes a single image stack will contain the spindle in which we are interested as well as microtubules from other cells nearby. To alleviate the contribution of this background, we manually select a polygonal region of interest (ROI) for each image stack, and all processing done refers only to the voxels in the ROI. For each image stack, a *z*-sum projection is computed and displayed; the ROI is manually selected from this representation. This *z*-sum ROI is used for all images in the stack. At present, with respect to the time required to prepare cells and acquire images, this manual processing is not a limitation. As we intend to move toward high-throughput analysis in ongoing efforts, automatically detecting and isolating the spindle from the background will become a future topic of research.

3.1 *Intensity Features*

The intensity values in our data are proportional to the fluorescent signal intensity in a voxel and therefore represent the density of tubulin in that voxel. We consider a voxel whose center is located at (x,y,z) and with intensity represented by $v(x,y,z)$. The intensity value is given approximately by

$$v(x,y,z)=\int_{x-\Delta x/2}^{x+\Delta x/2}\int_{y-\Delta y/2}^{y+\Delta y/2}\int_{y-\Delta y/2}^{y+\Delta y/2}\rho(x,y,z)dx\,dy\,dz, \quad (1)$$

where $(\Delta x,\Delta y,\Delta z)$ are the voxel dimensions and $\rho(x,y,z)$ is the local fluorescent marker, and hence tubulin, concentration. Assuming that $\rho(x,y,z)$ is approximately constant across the voxel, we get

$$v(x,y,z)=\Delta x\Delta y\Delta z\rho(x,y,z). \quad (2)$$

Since our images were captured with constant voxel dimensions and microscope settings, and our preparations were made consistently, intensity-based features may indicate variations in tubulin concentration that are of interest to the biologist. Please see Sec. 3.3, however, regarding caveats on the use of intensity features. Of the 49 features in our complete set, we compute eight such intensity features as described next.

F01: *Mean*. The mean gray value μ of all voxels. A higher mean value may indicate a higher concentration of tubulin in the mitotic spindle.

F02: *Standard deviation*. The standard deviation σ of all voxels. A high standard deviation may indicate a very irregular distribution of tubulin in the mitotic spindle.

F03: *Histogram skewness*. The skewness ψ is a measure of the asymmetry of a distribution.[24] A low skewness value indicates a nearly symmetric distribution, while a high skewness value indicates a very asymmetric distribution. Skewness is given by

$$\psi=\frac{m_3}{m_2^{3/2}}, \quad (3)$$

where m_q is the q'th central moment. For our discrete distributions, where we have bins given by $b(i)$ and bin masses or probabilities given by $p(i)$, the central moments are computed according to

$$m_q=\sum_n [b(i)-\mu]^q p(i), \quad (4)$$

where μ represents the distribution mean and is given simply by $\mu=\Sigma_i b(i)p(i)$. For the histogram, $b(i)\in[0,255]$ represents the 8-bit gray value and $p(i)$ is the number of voxels of gray level $b(i)$ divided by the total number of voxels. Characteristics of the histogram, as measured by this feature and F04 through F08, may indicate more subtle variations in tubulin distribution than captured by features F01 and F02 alone.

F04: *Histogram kurtosis excess*. The kurtosis excess is a measure of how peaked a distribution is.[24] Low values indicate a "flat" distribution, while high values indicate a distribution with a strong peak. Kurtosis excess is defined by

$$\kappa=\frac{m_4}{m_2^2}-3. \quad (5)$$

With this definition, the normal (Gaussian) distribution has $\kappa=0$, while an exponential distribution has $\kappa=6$.

F05 through 08: *Histogram principal component analysis coefficients*. We represent each histogram as a 256-

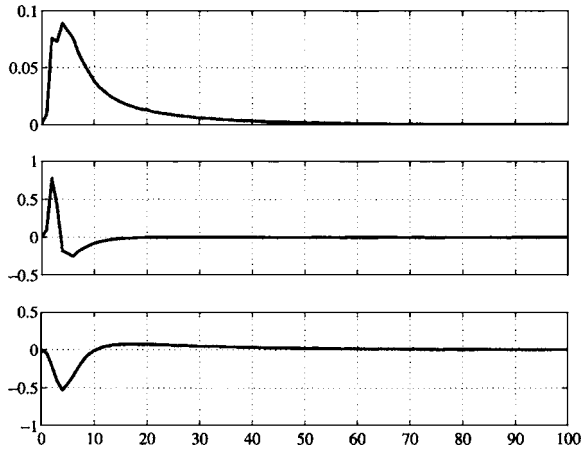

Fig. 3 Principal component analysis of the histograms. From top to bottom, the curves represent the mean histogram and first two principal components, respectively. Recall that the mean histogram is subtracted from every histogram prior to PCA and that the principal components are orthonormal basis vectors with both positive and negative values. Only the gray-level range from [0 100] is shown because the values from [101 255] are very small relative to those on [0 100].

dimensional vector (for the [0, 255] gray-value range) and then perform principal component analysis (PCA)[25] on the collection of histograms. Note that the first step in PCA is to subtract the ensemble mean histogram, which implies that there will be negative values in the resulting vectors. The computed principal components form an orthonormal basis for the ensemble; a sample histogram can be reconstructed as a weighted sum of these basis vectors added to the ensemble mean. We keep as features the PCA coefficients corresponding to the first four principal components, which represent the four most significant shape variations in the histograms. The first four PCA coefficients then represent "how much" of the corresponding component is in a given histogram. In Fig. 3, we show the mean histogram and the first two principal components. Note in Fig. 3 that only the gray-level range from [0 100] is shown, as the values greater than [101 255] are quite small relative to those over [0 100].

3.2 *Structure Features*

We now turn our attention to features that are related to the mitotic spindle structure or morphology. Each of the features described in this section is related to the shape of the spindle and/or the 3-D tubulin distribution in the spindle. Since the spindles are in fact 3-D objects, and we cannot guarantee that they are all imaged in the same pose, we must first establish an internal coordinate system for each spindle stack. We let each voxel in the image stack represent a point mass with mass equal to the voxel's intensity value. For each spindle image stack, we compute the center of mass and the principal axes of inertia[26–28] to serve as the origin and axes, respectively, of a spindle-centric coordinate system.

The principal axes of inertia represent mutually orthogonal axes about which a rigid body can be dynamically balanced, meaning its angular velocity is parallel to its angular momentum. A rigid body that is imparted with an angular velocity in the direction of (i.e., made to spin about) a principal axis will continue to spin. The principal axes are given by the eigenvectors of the moment of inertia matrix

$$\mathbf{I} = \begin{pmatrix} I_{xx} & I_{xy} & I_{xz} \\ I_{xy} & I_{yy} & I_{yz} \\ I_{xz} & I_{yz} & I_{zz} \end{pmatrix}, \tag{6}$$

where the elements are computed as follows. Let $v(x_o, y_o, z_o)$ represent a voxel value in the image stack, (x_o, y_o, z_o) the physical coordinates in the original coordinate system, $(\bar{x}, \bar{y}, \bar{z})$ the center of mass relative to the original coordinate system, and $\mathcal{M}$ the total spindle mass (i.e., the sum of all the voxel intensities); then the elements of $\mathbf{I}$ are given by

$$I_{xx} = \left[\sum_{x_o} \sum_{y_o} \sum_{z_o} v(x_o, y_o, z_o)(y_o^2 + z_o^2) \right] - \mathcal{M}(\bar{y}^2 + \bar{z}^2), \tag{7}$$

$$I_{yy} = \left[\sum_{x_o} \sum_{y_o} \sum_{z_o} v(x_o, y_o, z_o)(x_o^2 + z_o^2) \right] - \mathcal{M}(\bar{x}^2 + \bar{z}^2), \tag{8}$$

$$I_{zz} = \left[\sum_{x_o} \sum_{y_o} \sum_{z_o} v(x_o, y_o, z_o)(x_o^2 + y_o^2) \right] - \mathcal{M}(\bar{x}^2 + \bar{y}^2), \tag{9}$$

$$I_{xy} = -\left[\sum_{x_o} \sum_{y_o} \sum_{z_o} x_o y_o v(x_o, y_o, z_o) \right] + \mathcal{M}\bar{x}\bar{y}, \tag{10}$$

$$I_{xz} = -\left[\sum_{x_o} \sum_{y_o} \sum_{z_o} x_o z_o v(x_o, y_o, z_o) \right] + \mathcal{M}\bar{x}\bar{z}, \tag{11}$$

$$I_{yz} = -\left[\sum_{x_o} \sum_{y_o} \sum_{z_o} y_o z_o v(x_o, y_o, z_o) \right] + \mathcal{M}\bar{y}\bar{z}. \tag{12}$$

We then compute the eigenvalues and eigenvectors of $\mathbf{I}$ and construct a new reference frame whose origin is at the center of mass and whose three axes are in the direction of the eigenvectors (i.e., the principal axes). The eigenvalues are known as the principal moments of inertia and we sort the axes in the new reference frame (x, y, z) in order of descending eigenvalues. Hence, a position (x_o, y_o, z_o) in the original coordinate system is transformed into (x, y, z) in the spindle-centric coordinate system by

$$\begin{pmatrix} x \\ y \\ z \end{pmatrix} = \begin{pmatrix} \mathbf{a}_1^T \\ \mathbf{a}_2^T \\ \mathbf{a}_3^T \end{pmatrix} \begin{pmatrix} x_o - \bar{x} \\ y_o - \bar{y} \\ z_o - \bar{z} \end{pmatrix}, \tag{13}$$

where the three-vector $\mathbf{a}_i$ represents principal axes i, given as coordinates in the original reference frame, sorted by descending eigenvalue. In Fig. 4, we illustrate the principal axes of inertia using a simple ellipsoidal model, which is a reasonable approximation of the 3-D spindle shape. In such an ellipsoid, the first principal axis would point in the direction of the narrowest part and the third principal axis would point in the direction of the longest part (pole to pole). For each spindle, we transform each voxel's coordinates into this spindle-centric coordinate system and then compute the shape-based features described next.

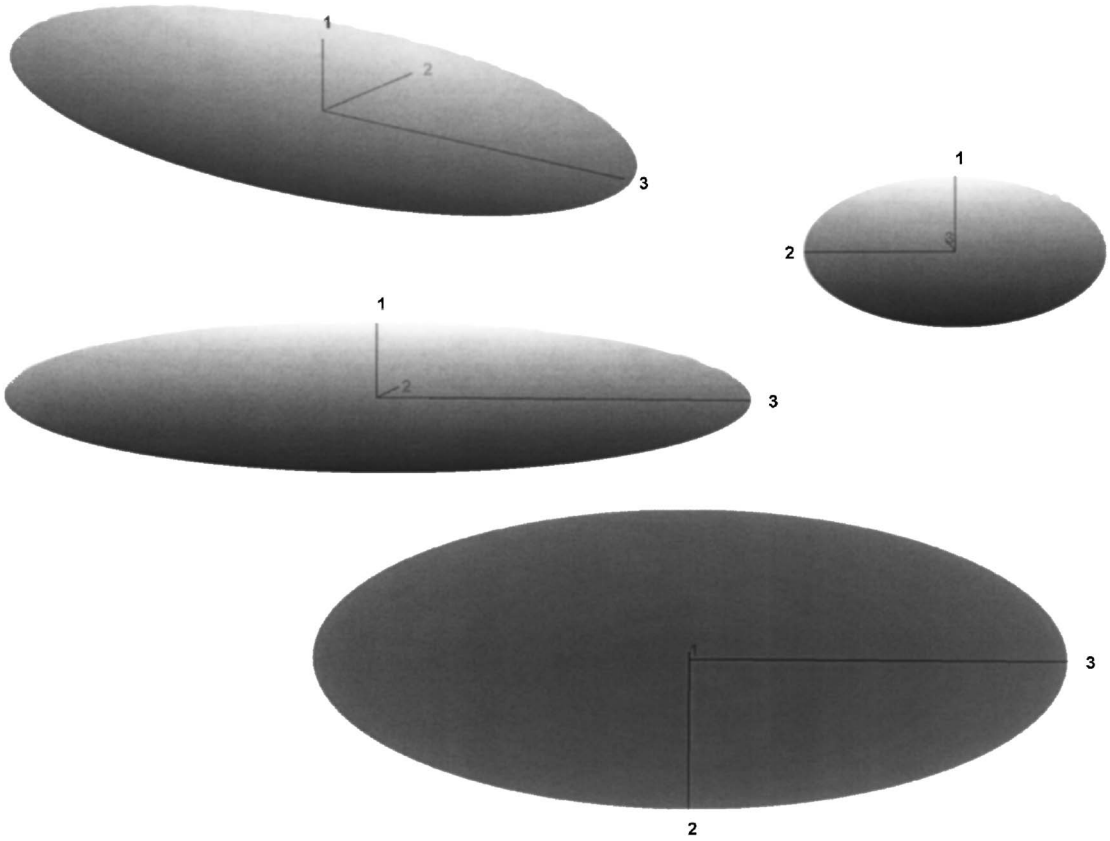

Fig. 4 Illustration of principal axes of inertia using an ellipsoidal model, where a uniform distribution of mass has been assumed (shading is only to enhance 3-D effect). The three axes are shown with lengths inversely proportional to their moments of inertia. Axis 3 corresponds to the pole-to-pole axis of the spindle. Axes 1 and 2 form the equatorial plate of the spindle (where the chromosomes align). The spindle represented by this model is somewhat flattened, with the spread along axis 1 being somewhat less than that along axis 2 (which implies a larger moment of inertia about axis 1). These illustrations all represent orthographic projections.

F09 through F12, F19 through F22, and F29 through F32: *Mass percentiles*. These features are the intervals in microns, along each principal axis, that enclose a certain percentage of the total spindle mass (i.e., tubulin content). They are computed as follows for axis 1 (and identically, with appropriate variable substitutions, for axes 2 and 3). Define N bins, X_k, along the first principal axis (i.e., axis 1) with centers at

$$x_k = x_{\min} + \frac{k-1}{N-1}(x_{\max} - x_{\min}), \tag{14}$$

for $k=1,\ldots,N$ and with bin width

$$\epsilon = \frac{x_{\max} - x_{\min}}{N-1}. \tag{15}$$

The k'th bin, X_k, is given by the interval $X_k=(x_k-\epsilon/2, x_k+\epsilon/2]$. In our experiments, described later in Sec. 4, we use $N=200$, and $x_{\min}$ and $x_{\max}$ are set to -10 and $+10$ μm, respectively. We now compute the projection of spindle mass onto axis 1, $p_1(x_k)$, as follows:

$$p_1(x_k) = \frac{1}{\mathcal{M}} \sum_{x \in X_k} \sum_{y} \sum_{z} v(x,y,z), \tag{16}$$

where $\mathcal{M}$ represents the total spindle mass. Note that the normalization by $\mathcal{M}$ provides invariance to intensity scaling of the image stack. An example of $p_1(x_k)$, computed for one spindle image stack, is shown in Fig. 5. Recalling the ellipsoidal model of Fig. 4, the first principal axis (i.e., x_k) is aligned along the shortest part of the spindle. In the spindle shown in Fig. 2, for example, axis 1 would approximately correspond with the optical axis, perpendicular to the plane of the page. The mass distribution along this axis hence describes the tubulin distribution in the spindle along the short axis of the spindle equatorial plate. Similar plots for $p_2(y_k)$ and $p_3(z_k)$ are shown in Figs. 6 and 7 for axes 2 and 3, respectively. Note that axis 3, which corresponds to the lowest principal moment of inertia, is oriented in the pole-to-pole direction of the spindle. Since tubulin concentrations tend to be higher at the poles, we can see in Fig. 7 that $p_3(z_k)$ tends to be bimodal, where the two peaks correspond to the poles. Since we are interested in variations in spindle morphology that may be asymmetric, we orient all of the axis 3 mass projections, $p_3(z_k)$, so that the larger peak is to the left (i.e.,

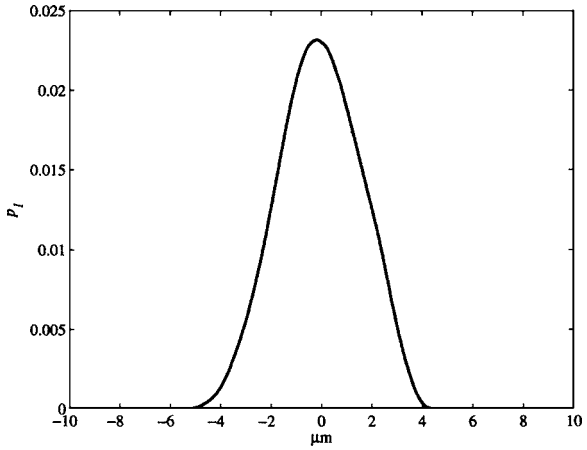

Fig. 5 Mass projected onto the first principal axes $p_1(x_k)$.

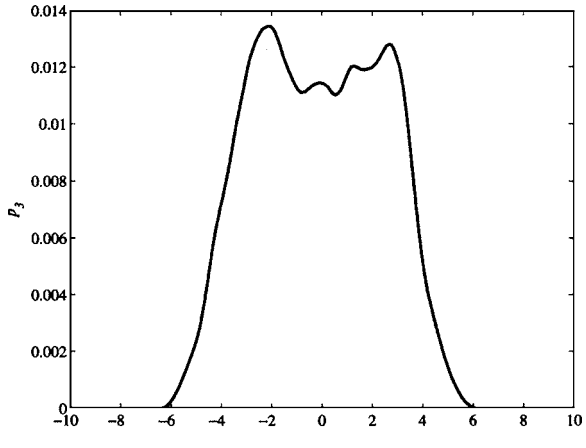

Fig. 7 Mass projected onto the third principal axes $p_3(x_k)$.

the positive side of axis 3 points toward the lower concentration peak).

An axis 1 mass percentile, $\Delta_1(f)$, is the minimum-width interval about $x=0$ in the spindle-centric coordinate system that contains the fraction f of the total mass and is computed as follows:

$$\Delta_1(f) = \arg\min_{\Delta}\left[\sum_{x_k\in[-\Delta/2,\Delta/2]} p_1(x_k)\right] > f. \qquad (17)$$

We compute and store $\Delta_1(f)$—as well as $\Delta_2(f)$ and $\Delta_3(f)$—for $f\in\{0.25,0.50,0.75,0.95\}$. These features represent the distribution of tubulin along the first, second, and third principal axes.

F13 through F16, F23 through F26, and F33 through F36: *Mass PCA coefficients*. We represent the mass projected onto each axis, $p_1(x_k)$, $p_2(y_k)$, $p_3(z_k)$ as N vectors and perform PCA on the collection of these vectors. We keep as features the four coefficients corresponding to the first four principal components. In Fig. 8 we show the mean projection of mass onto axis 1 and the first two principal components. Similar plots are shown for axes 2 and 3 in Figs. 9 and 10, respectively.

F17 and F27: *Axes 1 and 2 mass skewness*. The skewness, ψ_1 of the mass is projected onto axis 1, ψ_1, using Eqs. (3) and (4) with $p_1(x_k)$ representing the distribution and x_k the bins. Axis 2 is similarly computed. Because of the bimodality, we describe the axis 3 skewness and kurtosis computation separately.

F18 and F28: *Axes 1 and 2 mass kurtosis excess*. The kurtosis excess κ_1 of the mass is projected onto axis 1, $p_1(x_k)$, using Eqs. (4) and (5). Axis 2 is similarly computed.

F37: *Axis 3 mass kurtosis excess*. The kurtosis excess κ_3 of the mass is projected onto axis 3, $p_3(z_k)$, using Eqs. (4) and (5). Because of the bimodal nature, we only compute kurtosis excess for the entire curve. We then compute skewness and kurtosis excess for each side of the curve individually.

F38: *Axis 3 mass left-side skewness*. The skewness ψ_{3l} of $p_3(z_k)$ for $k=1,\ldots,N/2$.

F39: *Axis 3 mass left-side kurtosis excess*. The kurtosis excess κ_{3l} of $p_3(z_k)$ for $k=1,\ldots,N/2$.

F40: *Axis 3 mass right-side skewness*. The skewness ψ_{3r} of $p_3(z_k)$ for $k=N/2+1,\ldots,N$.

F41: *Axis 3 mass right-side kurtosis excess*. The kurtosis excess κ_{3r} of $p_3(z_k)$ for $k=N/2+1,\ldots,N$.

F42 through 45: *Radial mass percentiles about axis 3*.

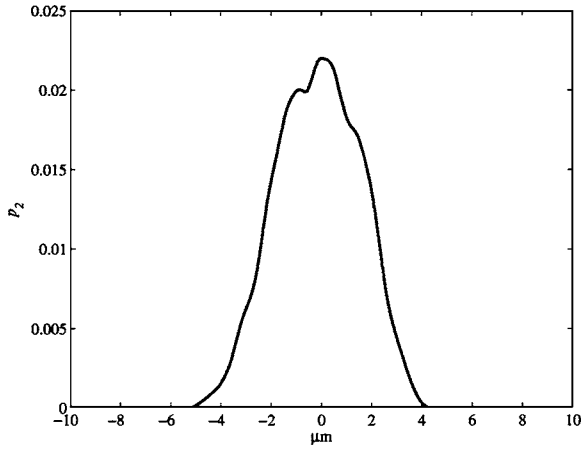

Fig. 6 Mass projected onto the second principal axes $p_2(y_k)$.

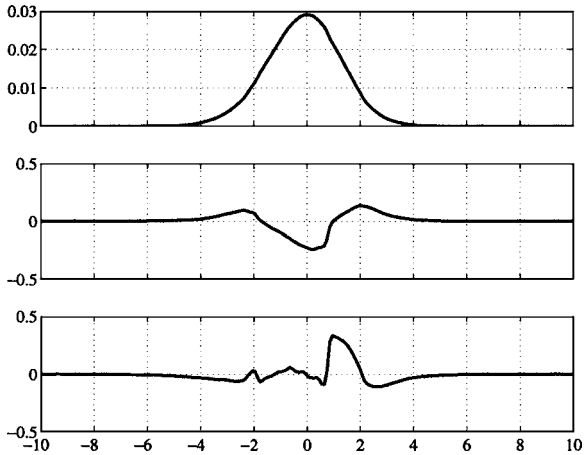

Fig. 8 Mean and first two principal components, from top to bottom, respectively, of mass projected onto the first principal axis.

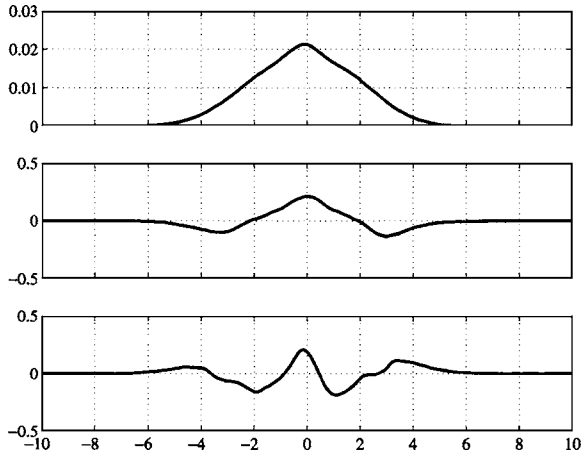

Fig. 9 Mean and first two principal components, from top to bottom, respectively, of mass projected onto the second principal axis.

With the final two sets of features (F42 through 45 and F46 through 49), we consider the radial distributions of spindle mass about axis 3. To achieve rotational invariance about axis 3, we represent $v(x,y,z)$ as $v(r,z)$, where $r=\sqrt{x^2+y^2}$. We construct P radial bins, B_i for $i=1,\ldots,P$, centered on

$$r_i = \frac{i-1}{P-1} r_{\max}, \tag{18}$$

and defined by $R_i=[r_i, r_{i+1})$. For features F42 through 45, we use $P=200$ and $r_{\max}=10$ μm. Similar to the computation for mass projected onto axis 1 (recall F09 through 12), we can then compute the radial distribution of the mass (about axis 3), for the entire spindle $p_r(r_i)$ as follows:

$$p_r(r_i) = \frac{1}{\mathcal{M}} \sum_{r \in R_i} \sum_{z} v(r,z), \tag{19}$$

where again $\mathcal{M}$ represents the total spindle mass. The radial mass percentiles $\Delta_r(f)$ are then given by

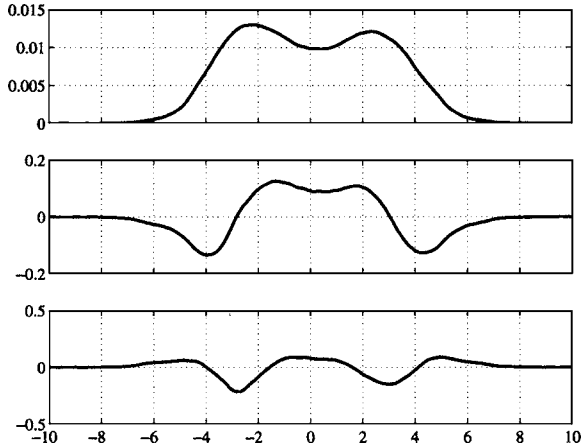

Fig. 10 Mean and first two principal components, from top to bottom, respectively, of mass projected onto the third principal axis.

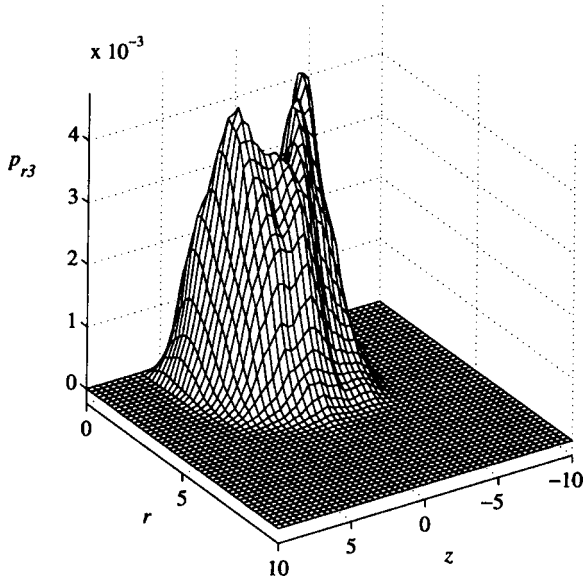

Fig. 11 Radial-axis 3 mass distribution p_{r3} shown as a surface plot.

$$\Delta_r(f) = \arg\min_{\Delta} \left[\sum_{r_i \leq \Delta} p_r(r_i) > f \right]. \tag{20}$$

In other words, $\Delta_r(f)$ is just the minimal radius enclosing the fraction f of the entire mass. We compute and store $\Delta_r(f)$ for $f \in \{0.25, 0.50, 0.75, 0.95\}$

F46 through 49: *Radial-axis 3 mass PCA coefficients*. In F42 through 45, we computed the radial distribution of the total spindle mass about axis 3. With features F46 through 49, we consider a similar radial distribution, but in "slices" that are parallel to axes 1 and 2 and placed along axis 3. We define radial bins again just as we did for F42 through 45 in Eq. (18). We also define bins Z_j along the third principal axis that are centered on

$$z_j = z_{\min} + \frac{j-1}{Q-1}(z_{\max} - z_{\min}), \tag{21}$$

with bin width

$$\delta = \frac{z_{\max} - z_{\min}}{Q-1}, \tag{22}$$

and given by $Z_j=(z_j-\delta/2, z_j+\delta/2]$. With these definitions, we define the radial-axis 3 mass distribution to be

$$p_{r3}(r_i, z_j) = \frac{1}{\mathcal{M}} \sum_{r_i \in R_i} \sum_{z_j \in Z_j} v(r,z). \tag{23}$$

Here we use $P=50$, $Q=50$, $r_{\max}=10$ μm, $z_{\min}=-10$ μm, and $z_{\max}=+10$ μm. This implies that the mass distribution $p_{r3}(r_i, z_j)$ is a 2-D, 50×50 array. In Fig. 11 we show an example of p_{r3} as a surface plot. The two peaks correspond to the spindle poles. We raster scan the 50×50 array making a 2500-dimensional vector and then perform PCA on the complete data from all spindles, keeping as features the first four PCA coefficients.

3.3 *Some Notes on the Features*

As noted in Sec. 3.1, we employ eight intensity-based features. We note, however, that such gray-level features would not necessarily be consistent across different laboratory and/or experimental settings. Such features would, in fact, vary under intensity scaling, which might be caused by changes in voxel dimensions, microscope settings, and/or preparation protocol. Our experimental results, discussed in Sec. 4, particularly the negative-control experiment of Sec. 4.6, support the use of such gray-level features within our own carefully controlled experimental conditions. In fact, in only one experiment—Sec. 4.4—do the intensity-based features comprise a significant number of the observed feature variations. Variations in intensity- or histogram-based features might prove useful under controlled conditions, as they might imply abnormalities in tubulin distribution that are not necessarily manifested in the structure-based features.

All of the structure-based features described in Sec. 3.2 characterize the spatial distribution of tubulin in the spindle. Statistical variations in these features indicate spatial variations in the tubulin distribution that are of biological significance, perhaps indicating phenotypic variation. The localization of such tubulin distribution variations to a specific region of the spindle may also indicate localized protein activity and/or protein-protein interaction. Currently, the localization of such structural variations (as characterized by statistically differing features) is done manually by examining the plots (e.g., mass projections) related to the varying features, as shown in Sec. 4.

We also note the invariance of the structural features to both intensity scaling and changes in voxel dimensions. As mentioned previously in Sec. 3.2 [see Eq. (16)] the morphology-based features are computed from mass distributions that have been normalized by the total spindle mass ($\mathcal{M}$). It should be readily apparent that this normalization provides intensity invariance for these features. Furthermore, recall that in doing the mass projections, we represent each voxel $v(x,y,z)$ as a point mass centered at (x,y,z) whose value is directly proportional to the voxel dimensions and the local tubulin concentration, as given by Eq. (2). For the mass projections, these point masses are projected onto much lower-resolution (by a factor of about 50) reference frames. Because of this, the morphology-based features are nominally invariant to changes in the voxel dimensions. For example, suppose we subdivide a single voxel of size $(\Delta x,\Delta y,\Delta z)$ into eight voxels of size $(\Delta x/2,\Delta y/2,\Delta z/2)$. Assuming that $\rho(x,y,z)$ is approximately constant over $(\Delta x,\Delta y,\Delta z)$, then each of the smaller voxels will have value equal to $1/8v(x,y,x)$. When doing the mass projections, however, the net contribution of either configuration will be equivalent. This also holds true as we increase the voxel size, so long as the voxel dimensions do not approach the bin sizes (which are about 50 times larger in this work) used for the mass projections.

Finally, we note that many of the features computed here are correlated. Recall, however, that discrimination is not the goal, but rather characterization and comparison. In fact, the correlation of some features in this endeavor is beneficial in helping to reduce contributions from uncorrelated noise across different spindle images.

4 Experimental Results

In this section, we present and discuss results of comparing the features from Sec. 3 for several datasets. The acquired experimental data comprised 44 images stacks from six cell types: the first three types are primary MEFs and the last three are immortalized MEFs, as described next.

1. Wild type (WT). Primary MEFs from normal (nonmutant) mice. Eight image stacks.
2. VPARP knockout (VPARP-KO). Primary MEFs, VPARP encoding gene is removed. Eight image stacks.
3. P53 knockout (P53-KO). Primary MEFs, p53 encoding gene is removed. Four image stacks.
4. Immortalized (IM). Immortalized MEFs derived from primary p53-KO MEFs. Eight image stacks.
5. Immortalized, Taxol treated at low concentration (IM-TaxLo). Immortalized MEFs derived from primary p53-KO MEFs, treated with 0.01-μM Taxol for 24 h. This serves as a positive control, since the anticancer drug Taxol is a tubulin poison and is known to give rise to structural effects on the spindle. Eight image stacks.
6. Immortalized, Taxol treated at a higher concentration (IM-TaxHi). Immortalized MEFs derived from primary p53-KO MEFs, treated with 0.1-μM Taxol for 24 h. Eight image stacks.

Images were obtained using a Leica SP2 laser scanning confocal microscope fitted with a 100× oil-immersion, plan apochromatic objective and using a pinhole setting of 0.9 airy units. The resulting image stacks contained voxels of approximately $0.03\times0.03\times0.08$-μm in size. Each image was 1024×1024 pixels and the stacks ranged from about 40 images deep to 100 images deep, depending on the size and/or pose of the imaged spindle. The 49 features described in Sec. 3 were computed for each of the 44 spindle image stacks.

We performed six different pair-wise comparisons of the datasets, including both positive control and negative control comparisons. For the comparisons, we used the two-sample t statistic[29] to determine if the individual feature means differed significantly between the datasets. We note as significant any features whose means were statistically different at $P<0.03$. For the t static, the P value represents the likelihood that the differences in the two means would be observed purely by chance. In other words, any observed differences in the feature means at $P<0.03$ would occur less than 3% of the time randomly. In the context of the 49 features that we compare, we expect that one or two features will almost always appear different at $P<0.03$, since $0.03\times49=1.47$. We discuss the six pair-wise comparisons in Secs. 4.1 through 4.6.

4.1 *Comparison 1: IM versus IM-TaxLo (Positive Control)*

Here we compared immortalized (IM) MEFs to IM MEFs that were treated with $0.01-\mu$M Taxol for 24 h. We found that 10 of the 49 features differed at $P<0.03$. We note that this comparison represents positive-control data, since the treatment with tubulin poison (Taxol) is known to affect the spindle structure, often in ways that are visually apparent to a biologist. We therefore expect to see statistically significant differences in several of our features. Since we found ten such features, which is significantly more than the one or two we

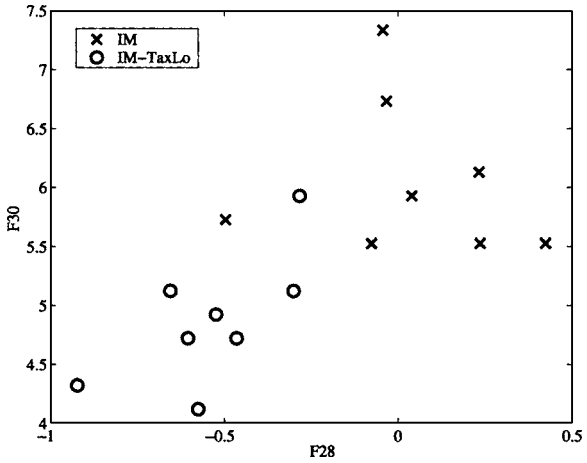

Fig. 12 Scatter plot of features F28 and F30 for the IM versus IM-TaxLo comparison of Sec. 4.1.

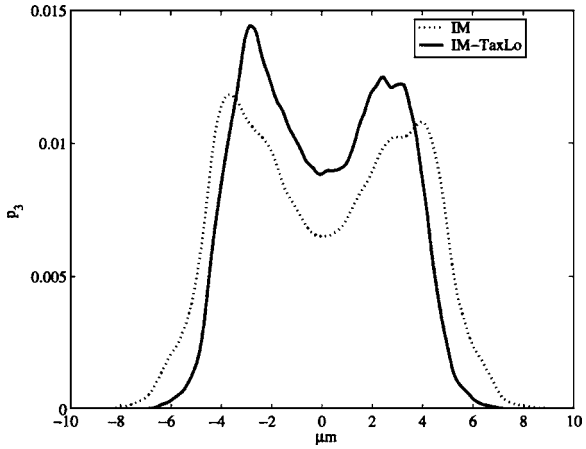

Fig. 14 Mean of axis 3 mass projections for the IM versus IM-TaxLo comparison of Sec. 4.1.

would expect randomly, we conclude that some of the differences in the treated versus untreated spindles are indeed captured by the features we have implemented.

The ten features that differed were F05, F28 through F34, F46, and F48. In Fig. 12, we show a scatter plot of features F28 and F30 for this comparison. F28 is the kurtosis excess of the axis 2 projected mass and F30 is the interval that contains 50% of the total spindle mass projected onto axis 3 (see Sec. 3.2). As we can see in Fig. 12, F28 for the IM-TaxLo data tends to be lower, indicating less peakedness than the IM data. This implies that the tubulin concentration along axis 2 is slightly lower near the spindle center in the Taxol treated cells. This indeed can be seen in Fig. 13, where we have plotted the mean axis 2 mass projections for both the IM and the IM-TaxLo data. Regarding F30 $[\Delta_3(0.5)]$, it is evident in Fig. 12 that it tends to be lower for the Taxol treated cells, indicating that these spindles are shorter along axis 3 (i.e., more concentrated toward the center) than the untreated cells. This can be seen in Fig. 14, where we have plotted the mean axis 3 mass projections for both the IM and the IM-TaxLo data. The shorter spindles reflect the consequences of the microtubules' inability to undergo polymerization/depolymerization due to the Taxol treatment.

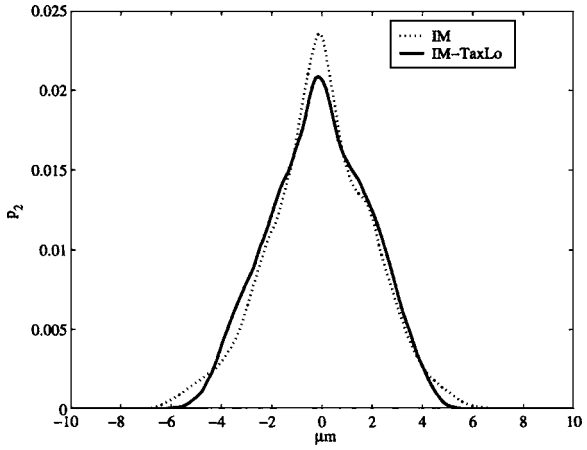

Fig. 13 Mean of axis 2 mass projections for the IM versus IM-TaxLo comparison of Sec. 4.1.

4.2 *Comparison 2: IM-TaxLo versus IM-TaxHi*

In this comparison, we were interested to see if the higher concentration of Taxol produced any significant spindle changes relative to the cells treated with a lower concentration of Taxol. We found only one feature that was different at $P < 0.03$, indicating that, according to our feature set, there are no statistically significant differences between the cells treated with low or high concentration of Taxol. In other words, at the Taxol concentrations tested, approximately equivalent changes were made to the spindle.

4.3 *Comparison 3: WT versus IM*

Here we compared normal MEFs to immortalized p53-KO MEFs. It has been shown that the absence of the p53 tumor suppressor gene can lead to spindles with multiple poles (as opposed to the normal two), which is a defect that is readily apparent to a human observer in spindle imagery (and can lead to cancer).[16] Although multipolar spindles were observed in the preparations, only bipolar IM spindle images were acquired for comparison. In other words, all of the IM spindle images we have used appear visually normal to a biologist.

In WT versus IM comparison, we found 26 features that differed at $P < 0.03$. These features were F01 through F05, F09 through F14, F22, F24, F28 through F33, F37 through F41, F46, and F47. Obviously the number of differing features seems to indicate significant differences between the normal (WT) and the IM cells. We note that this result is important, since abnormalities in normal-appearing, bipolar immortalized spindles have not been observed or reported to date. Several features related to the projection onto axis 3 are significantly different (F29 through F33, F37 through F41). We show in Fig. 15 the mean projections of mass onto axis 3 for the wild-type and IM cells. We can see from Fig. 15 that the poles of the IM spindles—represented by the two peaks in each curve—tend to be further apart (i.e., the IM spindles are longer) and the IM spindles tend to have less tubulin, relative to the poles, concentrated around their equatorial plates.

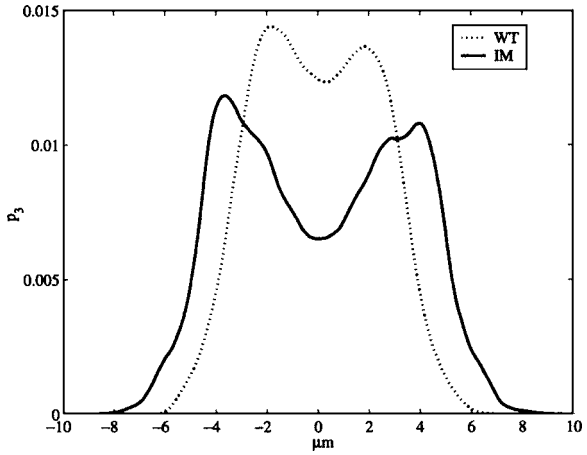

Fig. 15 Mean of the axis 3 mass projections for the WT versus IM comparison of Sec. 4.3.

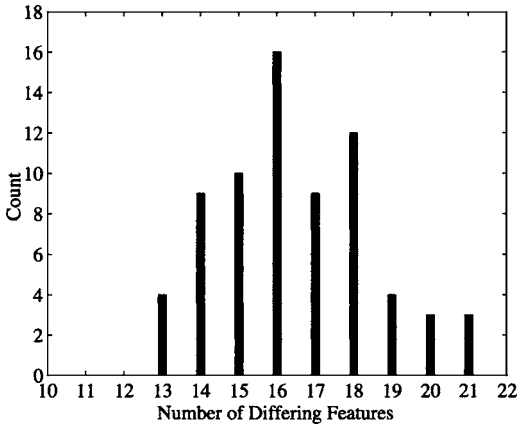

Fig. 17 Number of differing features for the 70 comparisons of WT versus p53-KO from Sec. 4.5. The mean number of differing features is 16.46 and the median is 16.

4.4 *Comparison 4: WT versus VPARP-KO*

In this comparison, we were interested to see if the computed features indicated any differences between normal (WT) spindles and VPARP-KO spindles in hopes of determining if VPARP has a role at the spindle. For the WT versus VPARP-KO comparison, we found six features that differed at $P<0.03$; these were F01, F02, F06, F07, F18, and F28. Since six features are more than the one or two we would expect to see purely by chance, this comparison seems to indicate that the VPARP-KO spindles are indeed different from the WT cells, but that the differences may be subtle. The difference of six features, however, is indeed significant when we consider the negative control experiment discussed in Sec. 4.6. We note that one of the differing features is F28, which is the kurtosis excess of the mass projected onto axis 2. In Fig. 16, we show the mean axis 2 projected mass of the wild-type cells and the VPARP knockout cells. It is apparent that the VPARP-KO cells are indeed flatter about the center of mass, indicating decreased tubulin concentration near the equatorial plate of the spindle. The results of this comparison may indicate a structural variation in the spindle, related to VPARP deficiency, that warrants further biological experimentation.

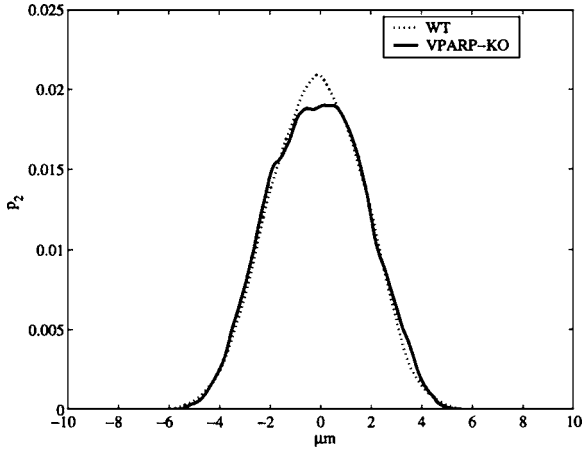

Fig. 16 Mean of the axis 2 mass projections for the WT versus VPARP-KO comparison of Sec. 4.4.

4.5 *Comparison 5: WT versus p53-KO*

Here we compared wild-type cells to p53-KO primary (i.e., not immortalized) cells. We compared the four p53-KO image stacks to every possible combination of four WT samples selected from the set of eight. For each of the 70 possible combinations, we performed the pair-wise feature comparison as discussed earlier and recorded the number of features differing with $P<0.03$. The results indicated that the mean number of differing features was 16.46 and the median number of differing features was 16. A histogram of the number of differing features is shown in Fig. 17, where we see the fewest number of differing features was 13 in four of the 70 cases. We note that, if one considers the chances of randomly observing different features, the observed spread in Fig. 17 is to be expected. Twelve specific features differed at $P<0.03$ in all 70 combinations; these were F20 through F23, F26, F29 through F33, F45, and F46. Many of these features are associated with the projections onto axes 2 and 3. We show in Figs. 18 and 19 the means of the projections onto axes 2 and 3, respectively, for the WT and p53-KO cells. These plots indicate that the p53-KO spindles are generally larger than the WT cells, having a longer pole-to-pole distance as well as a more uniform distribution of tubulin throughout the spindle structure (as opposed to pronounced peaks at the poles). Structural differences in such normal-appearing p53-KO spindles have not been previously observed by biologists. Some recent research,[30] however, indicates that p53 associates to centrosomes in mitosis, which might suggest the mechanism for such changes.

4.6 *Comparison 6: WT versus WT (Negative Control)*

In this final, negative-control comparison, we compared wild-type MEFs to wild-type MEFs. Since the cell types are the same, we expect there to be no significant differences in the features. We selected all possible subdivisions of the eight WT image stacks into two sets of four image stacks each; this results in 35 possible subdivisions. For each of the 35 possible combinations, we performed the pair-wise feature comparison

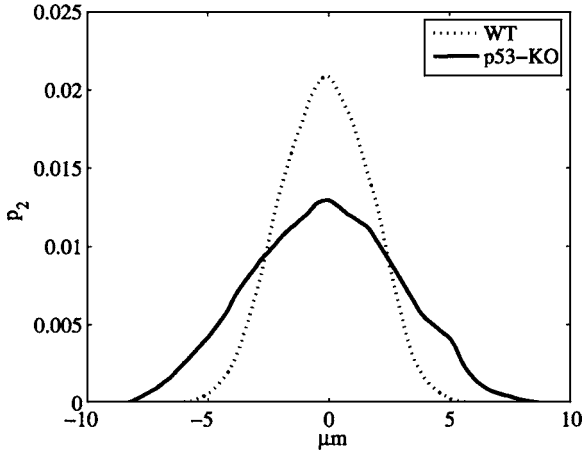

Fig. 18 Mean of the axis 2 mass projections for the WT versus p53-KO comparison of Sec. 4.5.

as discussed before and recorded the number of differing features. The results indicated that the mean number of differing features was 1.2 and the median number of differing features was in fact zero, as predicted. These results also indicate that the differences we have detected in the other comparisons are indeed significant, especially in the case of the WT versus VPARP-KO comparison, where only six features were found to differ with $P < 0.03$.

5 Conclusions

We describe an image analysis approach to detect quantitative differences in mitotic spindles that have been imaged, in 3-D, using confocal microscopy. This approach is based on a set of features or numerical descriptors that are computed from each 3-D image stack representing a spindle. Using these features, we compared several datasets that were characterized by different biological (genotype) and/or environmental (drug treatment) conditions. The experimental results on positive- and negative-control data (i.e., where we knew there should be significant differences or no differences, respectively) indicate that the proposed approach is indeed effective at detecting differences in spindle properties. Furthermore, in two of the experimental comparisons where mutant MEFs were compared to wild-type (normal) MEFs, the results indicate spindle differences that were previously unobserved by biologists.

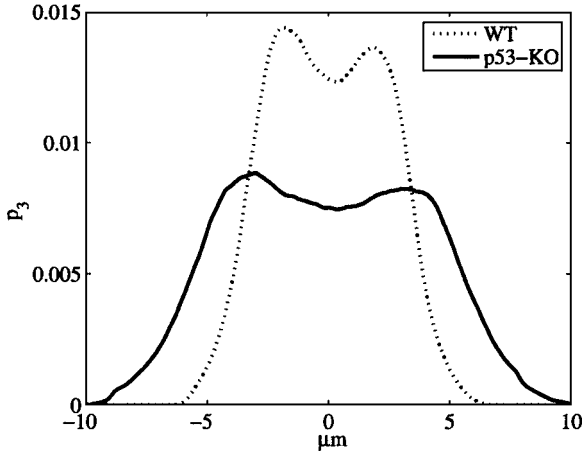

Fig. 19 Mean of the axis 3 mass projections for the WT versus p53-KO comparison of Sec. 4.5.

Finally, we note some directions of future research. The work presented was applied only to fixed-cell (i.e., nonliving) preparations. The mitotic spindle, however, is a dynamic structure. In future efforts, we will be imaging and analyzing spindles in living cells, where dynamic variations may also be uncovered. We also intend to apply the image analysis approach to additional gene-knockout models that are deficient in other spindle-associated proteins of interest. Finally, as a long-term goal, we plan to incorporate the methods developed here into a software tool to be used by cell biologists in their own laboratories and to provide for data exchange between different research groups.

Acknowledgments

The authors would like to acknowledge Lea Harrington and Bryan Snow, who directed the generation of a VPARP-deficient mouse model, and Dr. Atsushi Hirao for providing *p*53 deficient MEFs. We would like to thank Mark Ungrin, Philip Bingham, and Ken Tobin for their thorough reviews of this manuscript. We thank Conly Rieder for thoughtful and constructive discussions. We finally thank the anonymous reviewers whose constructive critiques helped us to significantly improve this work. Research sponsored by the Laboratory Directed Research and Development Program of Oak Ridge National Laboratory (ORNL), managed by UT-Battelle, LLC for the U.S. Department of Energy under contract number DE-AC05-00OR22725.

References

1. J. H. Hoh and P. K. Hansma, "Atomic force microscopy for high-resolution imaging in cell biology," *Trends Cell Biol.* **2**, 208–213 (July 1992).
2. J. G. McNally, T. Karpova, J. Cooper, and J. A. Conchello, "Three-dimensional imaging by deconvolution microscopy," *Methods* **19**(3), 373–385 (1999).
3. G. Kino and T. Corle, *Confocal Scanning Optical Microscopy and Related Imaging Systems*, Academic Press, New York (1996).
4. A. Diaspro, F. Beltrame, M. Fato, and P. Ramoino, "Characterizing biostructures and cellular events in 2D/3D," *IEEE Eng. Med. Biol. Mag.* **15**(1), 92–100 (1996).
5. A. Kramer, K. Neben, and A. Ho, "Centrosome replication, genomic instability and cancer," *Leukemia* **16**(5), 767–775 (2002).
6. K. Wood, W. Cornwell, and J. Jackson, "Past and future of the mitotic spindle as an oncology target," *Curr. Opin. Pharmacol.* **1**, 370–377 (2001).
7. E. O'Toole, M. Winey, and J. McIntosh, "High-voltage electron tomography of spindle pole bodies and early mitotic spindles in the yeast Saccharomyces cerevisiae," *Mol. Biol. Cell* **20**, 2017–2031 (1999).
8. D. Stephens and V. Allan, "Light microscopy techniques for live cell imaging," *Science* **300**(5616), 82–86 (2003).
9. C. Rieder and A. Khodjakov, "Mitosis through the microscope: advances in seeing inside live dividing cells," *Science* **300**(5616), 91–96 (2003).
10. J. Kaltschmidt, C. Davidson, N. Brown, and A. Brand, "Rotation and asymmetry of the mitotic spindle direct asymmetric cell division in the developing central nervous system," *Nat. Cell Biol.* **2**(1), 7–12 (2000).
11. T. Haydar, E. Ang, and P. Rakic, "Mitotic spindle rotation and mode of cell division in the developing telencephalon," *Proc. Natl. Acad. Sci. U.S.A.* **100**(5), 2890–2895 (2003).
12. S. Cutler and D. Erhart, "Polarized cytokinesis in vacuolate cell of Arabidopsis," *Proc. Natl. Acad. Sci. U.S.A.* **99**(5), 2812–2817 (2002).

13. J. Paluh, E. Nogales, B. Oakley, K. McDonald, A. Pidoux, and W. Cande, "A mutation in gamma-tubulin alters microtubule dynamics and organization and is synthetically lethal with the kinesin-like protein pkl1p," *Mol. Biol. Cell* **11**(4), 1225–1239 (2000).
14. J. Swedlow, K. Hu, P. Andrews, D. Roos, and J. Murray, "Measuring tubulin content in Toxoplasma gondii: a comparison of laser-scanning confocal and wide-field fluorescence microscopy," *Proc. Natl. Acad. Sci. U.S.A.* **99**(4), 2014–2019 (2002).
15. J. Price, D. Aykac, S. Gleason, K. Chourey, and Y. Liu, "Quantifying changes in the mitotic spindle structure caused by gene deficiency through image analysis," presented at *53rd Int. Fujihara Seminar: New Challenges in ADP-Ribose Metabolism*, July 2004.
16. K. Fukasawa, T. Choi, R. Kuriyama, S. Rulong, and G. F. Vande Woude, "Abnormal centrosome amplification in the absence of p53," *Science* **271**, 1744–1747 (Mar. 1996).
17. J. Fridman and S. Lowe, "Control of apoptosis by p53," *Oncogene* **22**(56), 9030–9040 (2003).
18. K. Vermeulen, Z. Berneman, and D. Van Bockstaele, "Cell cycle and apoptosis," *Cell Prolif* **36**(3), 165–175 (2003).
19. V. Kickhoefer, A. Siva, N. Kedersha, E. Inman, C. Ruland, M. Streuli, and L. Rome, "The 193-kD vault protein, VPARP, is a novel poly(ADP-ribose) polymerase," *J. Cell Biol.* **146**(5), 917–928 (1999).
20. M. Mossink, A. van Zon, R. Scheper, P. Sonneveld, and E. Wiemer, "Vault: a ribonucleoprotein particle involved in drug resistance?" *Oncogene* **22**(47), 7458–7467 (2003).
21. K. Suprenant, "Vault ribonucleoprotein particles: sarcophagi, gondolas, or safety deposit boxes?" *Biochemistry* **41**(49), 14447–14454 (2002).
22. A. van Zon, M. Mossink, R. Scheper, P. Sonneveld, and E. Wiemer, "The vault complex," *Cell. Mol. Life Sci.* **60**(9), 1828–1837 (2003).
23. Y. Liu, B. Snow, V. Kickhoefer, N. Erdmann, W. Zhou, A. Wakeham, M. Gomez, L. Rome, and L. Harrington, "A vault protein, VPARP, is associated with mammalian telomerase and is dispensable in telomerase function and vault structure in vivo," *Mol. Cell. Biol.* (in press).
24. J. Kenney and E. Keeping, *Mathematics of Statistics*, 3rd ed., Part 1, Chap. 7, pp. 100–103, Van Nostrand, New York (1962).
25. K. Fukunaga, *Statistical Pattern Recognition*, Morgan Kaufmann, New York (1990).
26. W. Flygare, *Molecular Structure and Dynamics*, Prentice-Hall, New York (1978).
27. J. Foote and A. Raman, "A relation between the principal axes of inertia and ligand binding," *Proc. Natl. Acad. Sci. U.S.A.* **97**, 978–983 (Feb. 2000).
28. S. Pei and L. Liou, "Using moments to acquire the motion parameters of a deformable object without correspondences," *Image Vis. Comput.* **12**, 475–485 (Oct. 1994).
29. D. S. Moore and G. P. McCabe, *Introduction to the Practice of Statistics*, 3rd ed., Freedman, New York (1999).
30. A. Tritarelli, E. Oricchio, M. Ciciarello, R. Mangiacasale, A. Palena, P. Lavia, S. Soddu, and E. Cundari, "p53 localization at centrosomes during mitosis and postmitotic checkpoint are ATM-dependent and require serine 15 phosphorylation," *Mol. Biol. Cell* **15**, 3751–3757 (Aug. 2004).